



RESEARCH ARTICLE

10.1002/2016JC012621

Long-term impacts of ocean wave-dependent roughness on global climate systems

Tomoya Shimura¹ , Nobuhito Mori¹ , Tetsuya Takemi¹ , and Ryo Mizuta² ¹Disaster Prevention Research Institute, Kyoto University, Kyoto, Japan, ²Meteorological Research Institute, Tsukuba, Japan

Key Points:

- Wave-dependent surface roughness was implemented within the Atmospheric GCM
- Wave steepness-dependent roughness and wave age-dependent roughness were considered
- The impacts of waves on atmospheric surface climatology and atmospheric circulation are presented

Correspondence to:

T. Shimura,
shimura.tomoya.2v@kyoto-u.ac.jp

Citation:

Shimura, T., N. Mori, T. Takemi, and R. Mizuta (2017), Long-term impacts of ocean wave-dependent roughness on global climate systems, *J. Geophys. Res. Oceans*, 122, doi:10.1002/2016JC012621.

Received 8 DEC 2016

Accepted 16 FEB 2017

Accepted article online 20 FEB 2017

Abstract Ocean surface waves can play an active role in climate systems, but they are often ignored in Global Climate Models (GCMs). Wave-dependent surface roughness was implemented within the Atmospheric GCM (MRI-AGCM) using the spectral wave model WAVEWATCH III. Two types of wave-dependent roughness, due to wave steepness and to wave age, were considered. Climate simulations with wave-dependent roughness were compared to simulations with just wind speed-dependent roughness. In climate simulation with wave steepness-dependent roughness, the spatial distribution of roughness is correlated to that of swell dominance. In simulation with wave age-dependent roughness, the spatial distribution of roughness is correlated to that of wind direction stationarity. Both simulations show reduced roughness in the tropics, which leads to an enhancement of surface wind speeds by up to 15%; these enhanced wind speeds are closer to observations compared with the baseline simulation with just wind speed-dependent roughness. We find that the reduced roughness and the enhanced wind speeds in the tropics lead to significant changes in atmospheric circulation, as in Hadley circulation and precipitation. The characteristic responses of the Hadley circulation and precipitation to changing sea surface roughness are presented.

1. Introduction

A number of studies have been conducted to understand the underlying mechanisms and assess the impact of climate change as well as to produce future climate projections. Climate studies are largely based on climate simulations using Global Climate Models (GCMs). GCMs which include realistic climate physics are required to obtain reliable climate simulations. Ocean surface gravity waves are driven by ocean surface winds; thus the wave climate is considered to be a passive component in the atmosphere-ocean climate system. The wave climate is simulated by a wave model, which uses the ocean surface winds from a GCM as forcing [e.g., *Hemer and Trenham*, 2016; *Shimura et al.*, 2016].

However, the wave climate is not only controlled in this direction, from the atmosphere to the ocean through ocean surface wind; waves are actually the product of a two-way feedback between the atmosphere and ocean [*Cavaleri et al.*, 2012]. The momentum, kinetic energy, and heat flux at the atmosphere-ocean interface may depend on the wave state [*Cavaleri et al.*, 2012]. However, wave-dependent physical processes are either parameterized simply using ocean surface winds or are not considered in almost all GCMs. For example, a sea surface roughness length can be used as a lower boundary condition in atmospheric modeling; this roughness length is assumed to be a function of factors such as wave age [*Drennan et al.*, 2003] and wave steepness [*Taylor and Yelland*, 2001]. It has been generally represented as a function of just wind speed in GCMs. An inaccurate or overly simplified sea surface roughness parametrization is likely to contribute to systematic errors in the large-scale circulations within GCM simulations [*Polichtchouk and Shepherd*, 2016].

Several previous studies of global climate simulations considered wave-dependent sea surface roughness in their models [*Weber et al.*, 1993; *Janssen and Viterbo*, 1996; *Fan et al.*, 2012; *Charles and Hemer*, 2013]. *Weber et al.* [1993] and *Janssen and Viterbo* [1996] conducted wave-atmospheric coupled climate integrations under winter conditions for a specific year. *Janssen and Viterbo* [1996] showed that the wave climate had a significant impact on atmospheric climate, especially at middle to higher latitudes, but *Weber et al.* [1993] concluded that ocean waves do not affect large-scale atmospheric circulations. *Fan et al.* [2012] developed a high-resolution atmosphere-wave coupled model which demonstrated good agreement with observations of wave heights; however, they did not address the feedback from waves to the atmosphere. *Charles and Hemer* [2013]

© 2017. The Authors.

This is an open access article under the terms of the Creative Commons Attribution-NonCommercial-NoDerivs License, which permits use and distribution in any medium, provided the original work is properly cited, the use is non-commercial and no modifications or adaptations are made.

implemented wave-dependent roughness into a coupled atmosphere-ocean model and showed that this coupling can impact sea surface climatology such as the surface wind speed and heat flux. These climate simulations all used different wave-dependent roughness parameterizations by *Janssen* [1991], *Fan et al.* [2012], *Taylor and Yelland* [2001], *Drennan et al.* [2003], or *Jones and Toba* [2001] for different GCMs. Therefore, the general impact of wave-dependent roughness on climate systems is not well understood.

The goal of this paper is to clarify how wave-dependent roughness impacts atmospheric climate systems. We implement the WAVEWATCH III wave model [Tolman, 2014] into the atmospheric GCM (MRI-AGCM) model [Mizuta et al., 2012]. The wave-atmosphere interaction is modeled as a wave-dependent momentum roughness; two different parameterizations for the wave-dependent momentum roughness are used in the simulations. Fifty years of climate simulations are carried out with the two parameterizations and for wind speed-dependent roughness. The impacts of wave-dependent roughness on the atmospheric climate system are investigated by comparing the wave-dependent simulations with those that have only wind-dependent roughness. We show that the spatial distribution of roughness climatology clearly depends on the chosen parameterizations and the differences in roughness climatology affect ocean surface wind climatology. Finally, we describe how wave-dependent effects can impact atmospheric circulation. The term “climatology” means overall average over the 50 years simulation period, hereafter.

Ocean surface currents can also modulate ocean-atmosphere momentum flux and affect climate system [e.g., Luo et al., 2005; Jungclaus et al., 2006]. We do not consider ocean circulation in this study in order to detect impacts of wave-dependent roughness on atmospheric climate. Investigation of impacts on atmosphere-ocean climate is the next step of this study.

2. Model and Experiment Description

2.1. GCM

For our simulations, we used the MRI-AGCM developed by the Japanese Meteorological Research Institute of the Japan Meteorological Agency. The output of MRI-AGCM climate simulations has been used for studies of climate change impact assessment on tropical cyclones [Murakami et al., 2012], storm surges [Yasuda et al., 2014], and ocean waves [Shimura et al., 2016]. The MRI-AGCM is a global spectral model, and the dynamical processes are computed in wave number space; the maximum triangular wave number is 159. The physical processes are computed in grid space; the horizontal grid is 320×160 , corresponding to a resolution of approximately 1.125° in both longitude and latitude. The model has 48 vertical layers. Although the MRI-AGCM can be operated with a finer resolution of 20 km [Mizuta et al., 2012], we adopted this coarser resolution to reduce computational costs. The surface processes in the MRI-AGCM are described below. A detailed description of the MRI-AGCM can be found in Mizuta et al. [2012].

The momentum and heat fluxes are represented as follows:

$$u_*^2 = C_m U^2 \tag{1}$$

$$-u_* \theta_* = C_h U \Delta \theta, \tag{2}$$

where u_* is the friction velocity, θ_* is the temperature scale, U is the sea surface wind speed, $\Delta \theta$ is the difference in potential temperature between the air and ground, and C_m, C_h are the bulk transfer coefficients for momentum and heat. The bulk transfer coefficients can be represented based on the Monin-Obukhov similarity theory:

$$C_m = \frac{\kappa^2}{\left[\log \left(\frac{z}{z_{0m}} \right) - \psi_m \left(\frac{z}{L} \right) \right]^2} \tag{3}$$

$$C_h = \frac{\kappa^2}{\left[\log \left(\frac{z}{z_{0m}} \right) - \psi_m \left(\frac{z}{L} \right) \right] \left[\log \left(\frac{z}{z_{0h}} \right) - \psi_h \left(\frac{z}{L} \right) \right]}, \tag{4}$$

where κ is the von Karman constant ($=0.4$), L is the Monin-Obukhov length, z is height, $\psi_m \left(\frac{z}{L} \right), \psi_h \left(\frac{z}{L} \right)$ are the integrated similarity functions representing the deviation from the logarithm law, and z_{0m}, z_{0h} are the roughness lengths for momentum and heat. The momentum roughness length is represented as follows:

Table 1. Experiment Description

Exp. Name	Wave	Roughness	Time FRAME (Initial Conditions)	Spatial Resolution, GCM/WAVE
CHA0001		$\alpha=0.001$		
CHA0005		$\alpha=0.005$		
CHA001	Off	$\alpha=0.01$	1990–2014 (2)	1.125°/–
CHA002		$\alpha=0.02$ (base line)		
CHA003		$\alpha=0.03$		
TY2001	On	<i>Taylor and Yelland</i> [2001]	1990–2014 (2)	1.125°/1.25°
DR2003	On	<i>Drennan et al.</i> [2003]	1990–2014 (2)	1.125°/1.125°

$$z_{0m} = 0.11 \frac{\nu}{u_*} + \alpha \frac{u_*^2}{g}, \quad (5)$$

where ν is the air dynamic viscosity coefficient and g is the gravitational acceleration. The first term of the right-hand side of equation (5) represents the roughness when the sea surface is smooth and wind speeds are low. The second term is the roughness of a rough sea surface (waves) represented by the Charnock relation. *Charnock* [1955] proposed a value of the Charnock coefficient $\alpha=0.018$; this value is tuned to 0.02 for the MRI-AGCM. In the Charnock relation, roughness increases with increasing wind speeds. This means that the sea surface conditions (waves) depend only on wind speed. Ocean wave effects are not considered in the heat roughness length (z_{0h}), which is set to $z_{0h}=0.62 \nu/u_*$.

2.2. Ocean Wave Model

The spectral wave model WAVEWATCH III (WW3) ver. 4.18 [Tolman, 2014] was used for wave computations. The spatial resolution is 1.125° or 1.25° (two different resolutions were due to computational costs) in both longitude and latitude in the global domain from 78°S to 75°N. The directional resolution is 10°. The frequency space of this model is 0.035–0.56 Hz, which is discretized in 30 logarithmic increments. The evolution of the spectral density of ocean waves results from a balance of three main sources for deep water conditions: wind input, wave dissipation, and nonlinear wave-wave interactions. The source term package from *Ardhuin et al.* [2010], called ST4, was used for the wind input and dissipation terms. The nonlinear wave interaction was calculated using the Discrete Interaction Approximation (DIA) [Hasselmann and Hasselmann, 1985].

2.3. Ocean Wave-Dependent Momentum Roughness Length

Here we introduce two types of wave-dependent momentum roughness lengths (z_{0m}) based on different physically motivated scaling [Drennan et al., 2005] and parameterized by either wave steepness [Taylor and Yelland, 2001] or wave age [Drennan et al., 2003]. *Taylor and Yelland* [2001] proposed a z_{0m} that is a function of wave steepness as follows:

$$\frac{z_{0m}}{H_s} = A_1 \left(\frac{H_s}{L_p} \right)^{B_1}, \quad (6)$$

where H_s is the significant wave height and L_p is the peak wavelength of the wave spectrum. A_1 and B_1 are tuning coefficients, and *Taylor and Yelland* [2001] chose $A_1=1200, B_1=4.5$ based on observations in the Dutch offshore region, the Baltic Sea, and Lake Ontario. *Drennan et al.* [2003] proposed a z_{0m} that is function of wave age as follows:

$$\frac{z_{0m}}{H_s} = A_2 \left(\frac{u_*}{c_p} \right)^{B_2}, \quad (7)$$

where c_p is the peak phase speed of the wind-sea component. *Drennan et al.* [2003] chose tuning coefficients $A_2=3.35, B_2=3.4$ based on observations from offshore Virginia, the Mediterranean, the North Sea, and Lake Ontario.

Note that the definitions of the spectral peaks for equation (6) are for the whole wave spectrum (denoted as total sea), while for equation (7) they are for the wind-sea component. Wind-sea component wave is generated and increased by wind, while swell is wave propagating away from the area where it was generated.

The total sea contains both wind-sea and swell components. *Drennan et al.* [2005] estimated the applicability of the two roughness parameterizations by comparing model results with various observations. They found that wave-dependent parameterizations yield improved estimates when compared with conventional wind speed-dependent parameterization. In particular, the wave steepness parameterization of equation (6) shows better results when wind-sea and swell waves coexist (a mixed sea), and the wave age parameterization of equation (7) is better for developing wave conditions (a young sea) [*Drennan et al.*, 2005].

Here we rewrite equations (6) and (7) in terms of the Charnock relation (the second term on the right-hand side of equation (5)) to highlight the differences between them. The linear dispersion relation for deep water conditions is as follows:

$$c = \frac{g}{2\pi} T = \sqrt{\frac{g}{2\pi}} L, \quad (8)$$

where c is the phase speed, T is the wave period, and L is the wavelength. The wind-sea relationship under equilibrium conditions is taken to be the Toba 3/2 power law [*Toba*, 1972] as follows:

$$\frac{gH_s^{eq}}{u_*^2} = \alpha_T \left(\frac{gT_s^{eq}}{u_*} \right)^{3/2}, \quad (9)$$

where $\alpha_T = 0.062$. It is assumed here that equation (9) is always valid for the wind-sea component. We introduce the expression $H_s = a_h H_s^{eq}$, $L_p = a_l L_p^{eq}$ for mixed sea conditions with both wind-sea and swell waves; a_h and a_l represent deviations from pure wind-sea waves, i.e., the presence of swell. The significant wave period is derived from the peak wave period: $T_s^{eq} = C_t T_p^{eq}$. Therefore, equation (6) can be rewritten as:

$$z_{0m} = A_1 (2\pi)^{\frac{B_1+3}{2}} C_t^{\frac{3(B_1+1)}{2}} \alpha_T^{B_1+1} \frac{a_h^{B_1+1}}{a_l^{B_1}} \left(\frac{u_*}{c_p^{eq}} \right)^{\frac{B_1-3}{2}} \cdot \frac{u_*^2}{g} = \alpha_{TY2001} \cdot \frac{u_*^2}{g}. \quad (10)$$

In this expression, the Charnock-like coefficient (α_{TY2001}) is represented as the deviation from wind-sea waves ($a_h^{B_1+1}/a_l^{B_1}$) and the inverse wave age (u_*/c_p^{eq}). After assigning values to the coefficients ($A_1 = 1200$, $B_1 = 4.5$, $\alpha_T = 0.062$) and setting $C_t = 0.95$, the equation can be written as:

$$\alpha_{TY2001} = 0.18 \frac{a_h^{5.5}}{a_l^{4.5}} \left(\frac{u_*}{c_p^{eq}} \right)^{0.75}. \quad (11)$$

Similarly, equation (7) can be rewritten as:

$$z_{0m} = A_2 (2\pi)^{3/2} C_t^{3/2} \alpha_T a_h \left(\frac{u_*}{c_p^{eq}} \right)^{B_2-3/2} \cdot \frac{u_*^2}{g} = \alpha_{DR2003} \cdot \frac{u_*^2}{g}, \quad (12)$$

where $c_p = c_p^{eq}$. After assigning coefficient values ($A_2 = 3.35$, $B_2 = 3.4$, $\alpha_T = 0.062$) and setting $C_t = 0.95$, the equation becomes

$$\alpha_{DR2003} = 3.03 a_h \left(\frac{u_*}{c_p^{eq}} \right)^{1.9}. \quad (13)$$

Comparing equations (11) and (13), we see that both equations show Charnock-like coefficients that decrease with increasing wave age, but equation (11) is more affected by the deviation from wind-sea waves, while equation (13) is more affected by wave age. If a_h and $a_l = 1$, the Charnock-like coefficient approaches to 0.02 when inverse wave age is 0.053 and 0.071 for equations (11) and (13), respectively.

2.4. Wave-AGCM Coupling

Here we describe how the MRI-AGCM and WAVEWATCH III were coupled; Figure 1 shows the schematic view of the coupling procedures. Wind speed data (10 m above the surface, U_{10}) from the MRI-AGCM is sent to WAVEWATCH III, and U_{10} at t_k time is interpolated to the WAVEWATCH III spatial grid. The time integration from t_{k-1} to t_k is carried out in WAVEWATCH III using the U_{10} as a forcing. The roughness calculated from the ocean wave variables in WAVEWATCH III are then sent to the MRI-AGCM. The wave variables H_s , L_p , and c_p at t_k are interpolated to the MRI-AGCM horizontal grid, and these variables are used to calculate the roughness length (z_{0m}) using the methods outlined in *Taylor and Yelland* [2001] or *Drennan et al.* [2003]. The

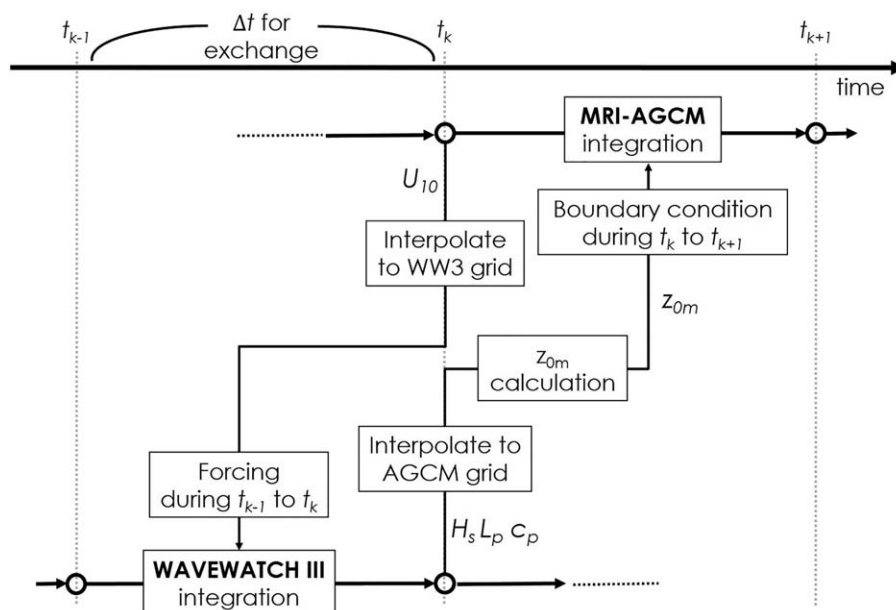


Figure 1. Schematic view of the coupling between MRI-AGCM and WAVEWATCH III.

time integration from t_k to t_{k+1} is then carried out in the MRI-AGCM using z_{0m} as the sea surface boundary condition. This coupling procedures to exchange variables are repeated every hour within the models.

2.5. Description of Numerical Experiments

Climate simulations were performed using both the wind speed-dependent and wave-dependent roughness parameterizations. The time frame of the climate simulations was the 25 year span from 1990 to 2014. Two climate simulations were performed changing the initial conditions of the model; thus data for a 50 year period is available from the simulations. The bottom boundary conditions are the sea surface temperature (SST) and sea ice extent taken from the Hadley Centre Global Sea Ice and Sea Surface Temperature (HadISST) data set [Rayner *et al.*, 2003]. Five climate simulations with wind speed-dependent roughness were performed using five different values for the Charnock coefficients ($\alpha=0.001, 0.005, 0.01, 0.02,$ and 0.03) to examine the uncertainty in the original Charnock parameterization. The baseline experiment has $\alpha=0.02$, which is the default value for the MRI-AGCM. Two climate simulations with wave-dependent roughness were performed based on equations (6) and (7). These series of experiments are denoted CHA0001, CHA0005, CHA001, CHA002, CHA003 for the wind speed-dependent roughness parameterization, and TY2001 and DR2003 for the wave-dependent roughness parameterizations; the experiments are summarized in Table 1.

3. Results and Discussion

Here we describe the impacts of the wave-dependent roughness implementations. Section 3.1 presents the direct impacts on surface climatology for C_m , and section 3.2 shows the impact on U_{10} . We provide insight into the consequent impacts on atmospheric circulation in section 3.3.

3.1. The Relationships Between Wind Speed and C_m

We show how the relationship between wind speed 10 m above the surface (U_{10}) and the bulk transfer coefficients for momentum (C_m) depend on the implementation of wave-dependent roughness. For example, Figure 2 shows this relationship at the middle to higher latitudes in the North Pacific (40°N – 50°N , 140°W – 180°W) and in the equatorial Pacific (5°S – 5°N , 140°W – 180°W); these two regions show largely different wave climatology, as will be discussed later. The C_m shown is for neutral conditions. Figure 2 shows a comparison between the results of our experiments (listed in Table 1) and the atmospheric reanalysis done by the European Centre for Medium-Range Weather Forecasts (ECMWF), the ERA-Interim [Dee *et al.*, 2011].

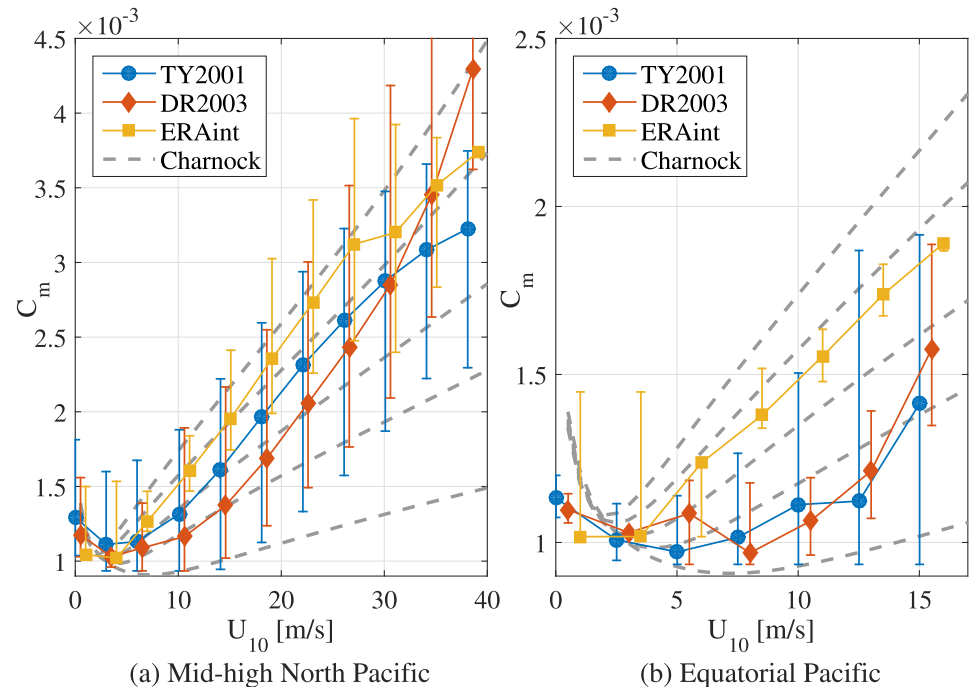


Figure 2. The relationship between C_m and U_{10} at (a) middle to high latitudes in the North Pacific and (b) in the equatorial Pacific. The five gray dashed lines (from top to bottom) are for CHA003, CHA002, CHA001, CHA0005 and CHA0001. The three colored lines with circles, diamonds, and squares are for TY2001, DR2003, and the ERA-Interim, respectively. The error bars indicate twice the standard deviations for each point.

The ECMWF numerical weather prediction model is the first operational coupled global atmospheric and wave model. The wave-dependent roughness (wave-dependent Charnock coefficient) in the ECMWF model is based on *Janssen* [1991].

In the experiments with wind-dependent roughness, C_m corresponds uniquely to wind speed. In the TY2001 and DR2003 experiments, C_m varies depending on the wave condition under a certain wind speed. At middle to higher latitudes in the North Pacific (Figure 2a), the mean value of C_m in TY2001 is close to that in CHA001 when wind speeds are low (up to 10 m/s); the TY2001 mean value of C_m comes closer to that in CHA002 when wind speeds increase. The mean value of C_m in DR2003 is lower than that in CHA001 when wind speeds are below 20 m/s and higher than that in CHA002 when wind speeds are greater than 35 m/s. This can be attributed to DR2003's sensitivity to wave age, indicated by equation (13). The relationships described above vary depending on the region considered because wave climates differ between regions. Figure 2b shows the relationship between wind speed and C_m in the equatorial Pacific. Here C_m for TY2001 and DR2003 are much lower than for CHA001; they are close to the values for CHA0005. The reason for the difference between Figures 2a and 2b, especially for TY2001, is that TY2001 is very sensitive to deviations from wind-sea waves, and these low latitude regions are swell-dominated and have lower wave steepness. The ERA-Interim has a mean value of C_m lower than that of CHA002 when wind speeds are below 15 m/s and larger when wind speeds increase. The variation in C_m (indicated by error bars in Figure 2) in the ERA-Interim is much smaller than the variations in C_m for TY2001 and DR2003 when wind speeds are lower than 15 m/s.

The regional dependence of C_m on the global scale is shown in Figure 3 as the spatial distribution of the mean C_m (C_m climatology) for winds speeds under 10–10.25 m/s for TY2001, DR2003 and the ERA-Interim. The C_m climatology from the climate simulations with wind speed-dependent roughness shows no spatial variation under same wind speeds. TY2001 and DR2003 show a clear dependence of C_m on region. TY2001's C_m tends to be smaller at low latitudes and smaller in the eastern region of each ocean (Figure 3a). This corresponds to the dominance of swell; a global view of swell probability can be seen in *Semedo et al.* [2011]. DR2003's C_m tends to be at a minimum at low latitudes and at a maximum at middle latitudes (30–40°) (Figure 3b). This is because small variations in the wind direction lead to older wave ages at low

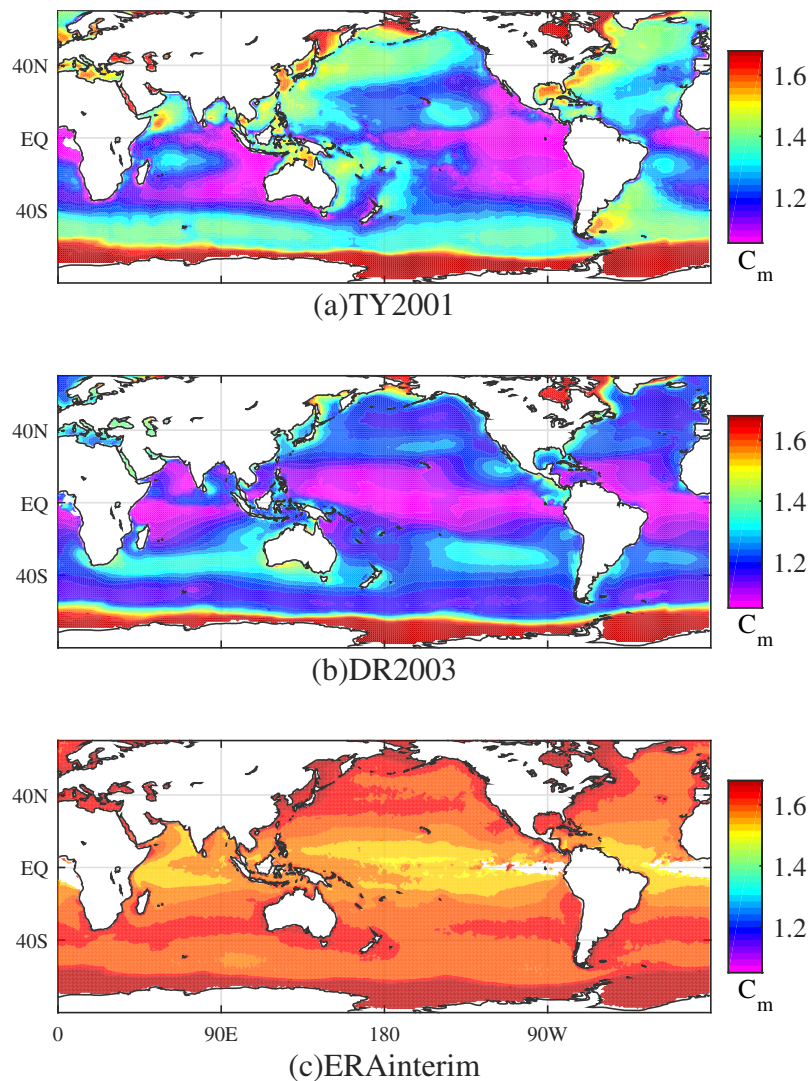


Figure 3. The spatial distribution of C_m climatology for wind speeds under 10–10.25 m/s in (a) TY2001, (b) DR2003, and (c) ERA-Interim.

latitudes; larger variations in wind direction lead to younger wave ages at middle latitudes (The wind direction stationarity is described in Appendix A). Although C_m values for the ERA-Interim show only small spatial contrasts (Figure 3c), the maximum C_m values are located at middle latitudes and have a spatial distribution similar to DR2003. The Charnock coefficient in the ECMWF model is represented by the spectral integration of wind input terms determined by the wind-sea component, so the spatial distribution of C_m for the ERA-Interim (Figure 3c) is similar to that of DR2003 (Figure 3b), but with much larger values and a much smaller spatial contrast than DR2003. Sensitivities to fetch of DR2003 and the ECMWF model [Janssen, 1991] are compared because Figures 3b and 3c is under same wind speed, 10–10.25 m/s. Given the JONSWAP spectrum [Hasselmann *et al.*, 1973] with $U_{10}=10$ m/s under neutral conditions, $C_m=1.45\times 10^{-3}$ for a 1 km fetch and 1.37×10^{-3} for a 100 km fetch in the ECMWF model, which are calculated by the method of Janssen [1991]. For DR2003, $C_m=2.59\times 10^{-3}$ for a 1 km fetch and 1.30×10^{-3} for a 100 km fetch; this confirms that the ERA-Interim shows a smaller spatial contrast of C_m than DR2003.

The spatial distribution of C_m in TY2001 and DR2003 (Figure 3) can be explained by the inverse wave ages (U_{10}/c_p). Note that phase speed is defined using the total sea peak for TY2001 and by the spectral peak of just the wind-sea component for DR2003. Figure 4 shows the inverse wave ages from the total sea peak compared to the wind-sea component peak. The total sea inverse wave age (Figure 4a) tends to be smaller

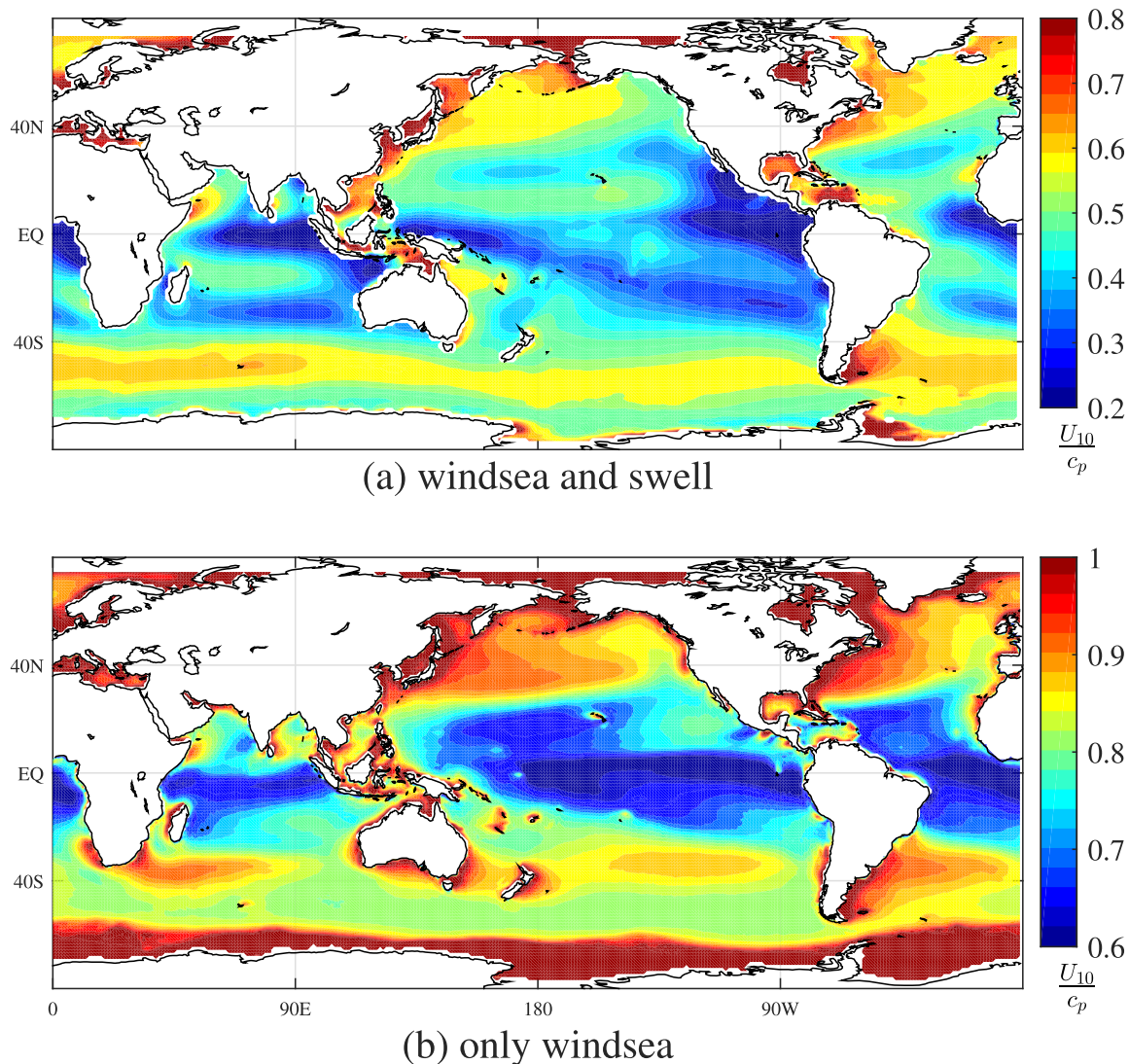


Figure 4. Inverse wave age climatology for phase speeds defined by (a) the total sea peak (TY2001) and (b) the spectral peak of the wind-sea component (DR2003).

at low latitudes and in the eastern regions of each ocean; this corresponds spatially to swell dominance [Semedo *et al.*, 2011] and to C_m in TY2001, shown by Figure 3a. The wind-sea component inverse wave age (Figure 4b) has maximum values at middle latitudes, especially in the Southern Hemisphere, and minimum values at low latitudes; this corresponds spatially to wind direction stationarity (Figure 12 in Appendix A) and to C_m in DR2003, shown by Figure 3b. Therefore, although the roughness length is defined by wave steepness and wave age for TY2001 and DR2003, respectively, the difference in spectral peak definition between the total sea and wind-sea component is more critical for the spatial distribution of C_m climatology. This is consistent with the discussion on difference between equations (11) and (13) in section 2.3.

3.2. Impacts on U_{10} Climatology

We show the impact that the distribution of C_m has on U_{10} climatology. Figure 5 shows the U_{10} climatology of CHA002 and the differences from CHA002 for CHA001, TY2001, and DR2003. For CHA001, U_{10} is globally 5% larger than that of CHA002. TY2001's U_{10} is 15% larger than U_{10} for CHA002 at low latitudes; U_{10} is similar for the two models at high latitudes, especially in the western parts of the ocean. The difference in U_{10} between TY2001 and CHA002 corresponds to the spatial contrast of C_m climatology (Figure 3a) and wave age (Figure 4a) seen in the western high latitudes and the eastern low latitudes. DR2003's U_{10} is 15% larger than CHA002 at low latitudes, especially in the western part of the ocean. The differences between U_{10} for

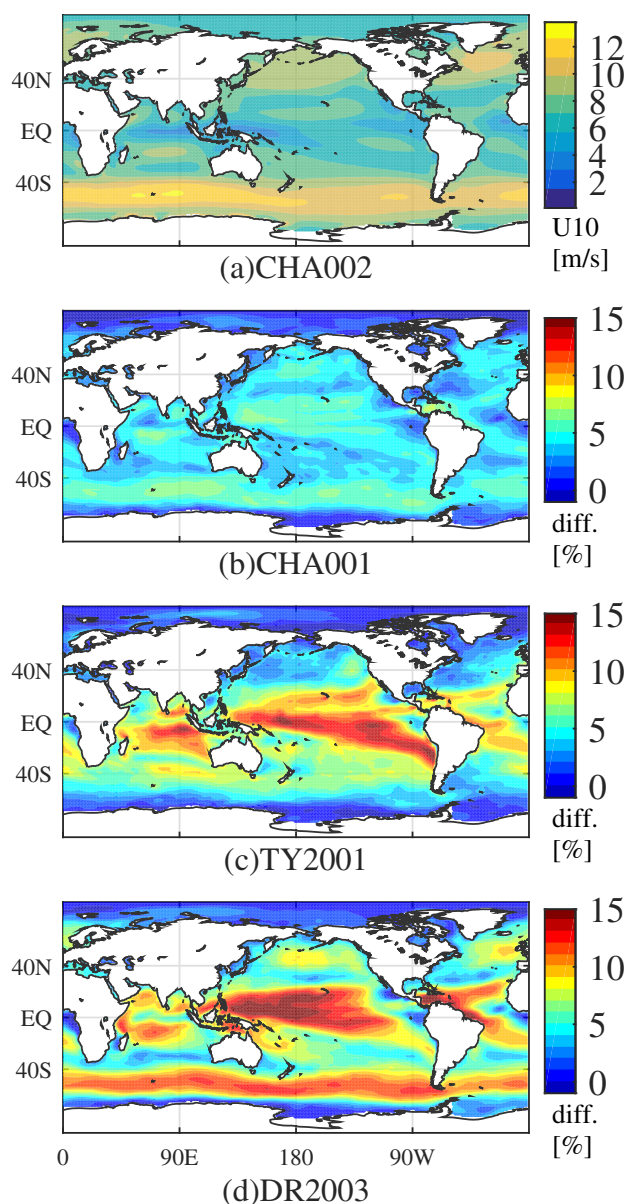


Figure 5. (a) U_{10} climatology (m/s) for CHA002. (b–d) The percent differences between CHA002 and CHA001, TY2001, and DR2003, respectively.

in the Southern Ocean because of smaller C_m of DR2003 than TY2001 around 50° latitudes (Figures 3a and 3b). TY2001 and DR2003 show good agreement with the observational data in low latitudes, while CHA002 clearly underestimates the wind speed by about 0.5 m/s. The climate simulations with wave-dependent roughness perform better for the wind speeds seen at low latitudes.

The climatological U_{10} differences, which depend on the choice of parameterizations, are clear in Figure 6. Differences in the momentum roughness length can weakly affect the heat transfer coefficient (C_h) without changing the heat roughness length in equation (4). We find that the differences in zonal mean sea surface heat flux among the different experiments are very small.

3.3. Impacts on Atmospheric Circulation

Here we describe how the differences in sea surface climatology can more generally impact atmospheric circulation. *Janssen and Viterbo* [1996] indicated that ocean wave implementation in the AGCM can change atmospheric circulation at middle and high latitudes, noting, for example, an equator-ward shift of a storm

CHA002 and DR2003 are small (5%) at middle latitudes and large (10%) at high latitudes; these differences correspond to the spatial contrast of C_m climatology (Figure 3b) and wave age (Figure 4b). These results indicate that differences in wave climatology lead to 1 m/s (15%) wind speed differences because of different sea surface roughness conditions.

The zonally averaged differences in U_{10} climatology among the experiments are in Figure 6. Several gridded global sea surface wind speed data sets, which are based on satellite observations, are also shown for reference in Figure 6, although satellite wind speed data are derived under a number of assumptions. The reference data are taken from the Objectively Analyzed air-sea Fluxes (OAF flux) project for 1990–2014 [Yu *et al.*, 2008], the National Oceanic and Atmospheric Administration (NOAA) Blended Sea Winds for 1988–2010 [Zhang *et al.*, 2006], the Hamburg Ocean Atmosphere Parameters and Fluxes from Satellite Data (HOAPS) for 1988–2008 [Fennig *et al.*, 2012], and the Version 3 Goddard Satellite-based Surface Turbulent Fluxes (GSSTF3) for 1988–2008 [Shie *et al.*, 2012]. Although there are some differences among the experiments and also among the observed data sets, the experiments with wave-dependent roughness overestimate wind speeds for middle to high latitudes by 1–2 m/s, especially in the Southern Ocean. Wind speeds of DR2003 are larger than those of TY2001 around 50° latitudes especially

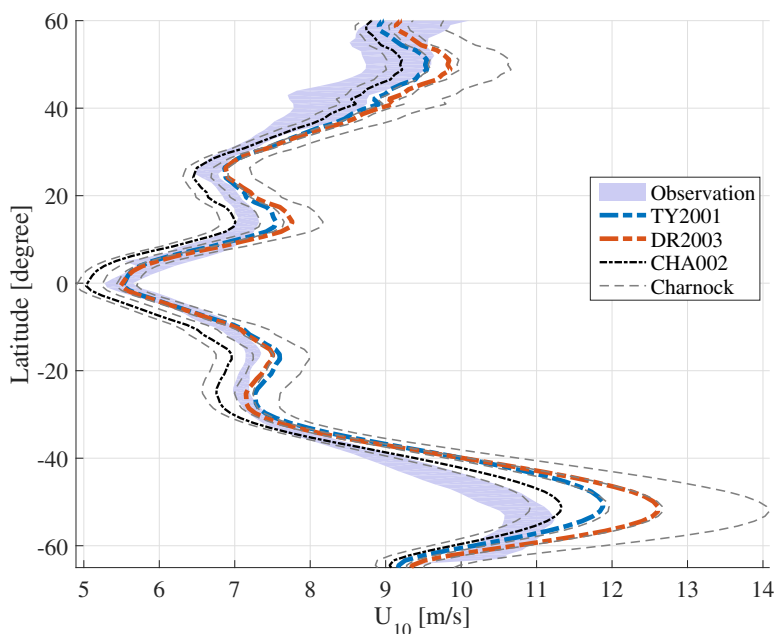


Figure 6. Zonally averaged U_{10} climatology. The two thick dashed lines show the results for TY2001 (blue) and DR2003 (red). The black dashed-dotted line is CHA002. The thin dashed lines (from left to right) are CHA003, CHA001, CHA0005, and CHA0001. The shading shows range of four satellite-based observations.

track in the Southern Ocean. Here we focus on how precipitation and Hadley circulation are affected by ocean wave implementation. Results for boreal summer (June–August, JJA) and winter (December–February, DJF) are presented below.

3.3.1. JJA Season

Figures 7a–7d show the boreal summer (JJA) precipitation climatology for CHA002 and the differences of CHA0001, TY2001, and DR2003. The differences show a characteristic spatial pattern in Figures 7b–7d. Positive deviations can be seen north of the Equator (approximately 0°N to 15°N) in the Pacific and East Asia. Negative deviations are seen south of the Equator (approximately 0°S to 15°S) in the western Pacific and the Indian Ocean. Negative deviations are also prominent around Central America and the extratropics of the western North Pacific. The maximum differences in precipitation are about 2 mm/d. The other experiments using the Charnock formula (CHA0005 and CHA001) have spatial patterns similar to those in Figures 7b–7d with magnitudes that vary correspondingly with the Charnock parameter; CHA003 shows a similar spatial pattern with the inverse sign because its Charnock parameter is larger than that of CHA002. Zonal mean precipitation differences between CHA002 and the other experiments are shown in Figure 8a. It is clear that the signs of the precipitation differences are opposite in the tropics south and north of the Equator. Among the experiments with wind speed-dependent roughness (different Charnock parameters), the precipitation differences correspond well with the magnitude of the Charnock parameter. For regions in East Asia and the western Pacific (approximately 90°E to 180°E), the precipitation differences between areas north and south of the Equator are more prominent.

The Hadley circulation can be depicted using zonal mean mass stream functions [Oort and Yienger, 1996]. Figure 8b shows the Hadley circulation (mass stream function) for CHA002 in JJA. The southern part of the Hadley circulation (anticlockwise circulation) is usually stronger in JJA than the northern (clockwise) circulation. The Hadley circulations differences between the experiments have large-scale features. The differences in the Hadley circulations are shown by applying Empirical Orthogonal Function (EOF) analysis [Von Storch and Zwiers, 2002] to the covariance matrix of the zonal mean mass stream functions of the seven experiments. The color scale in Figure 8b shows the first EOF mode, which is representative of the pattern of differences in Hadley circulation among the seven experiments. The first mode shows 87% variance, which indicates that the first mode is the dominant spatial pattern of the difference. When EOF analysis was performed for only the experiments with wind speed-dependent roughness, similar results were obtained. The coefficients of the first mode are 1.79, 0.38, -0.29 , -0.98 and -1.51 for CHA0001, CHA0005, CHA001,

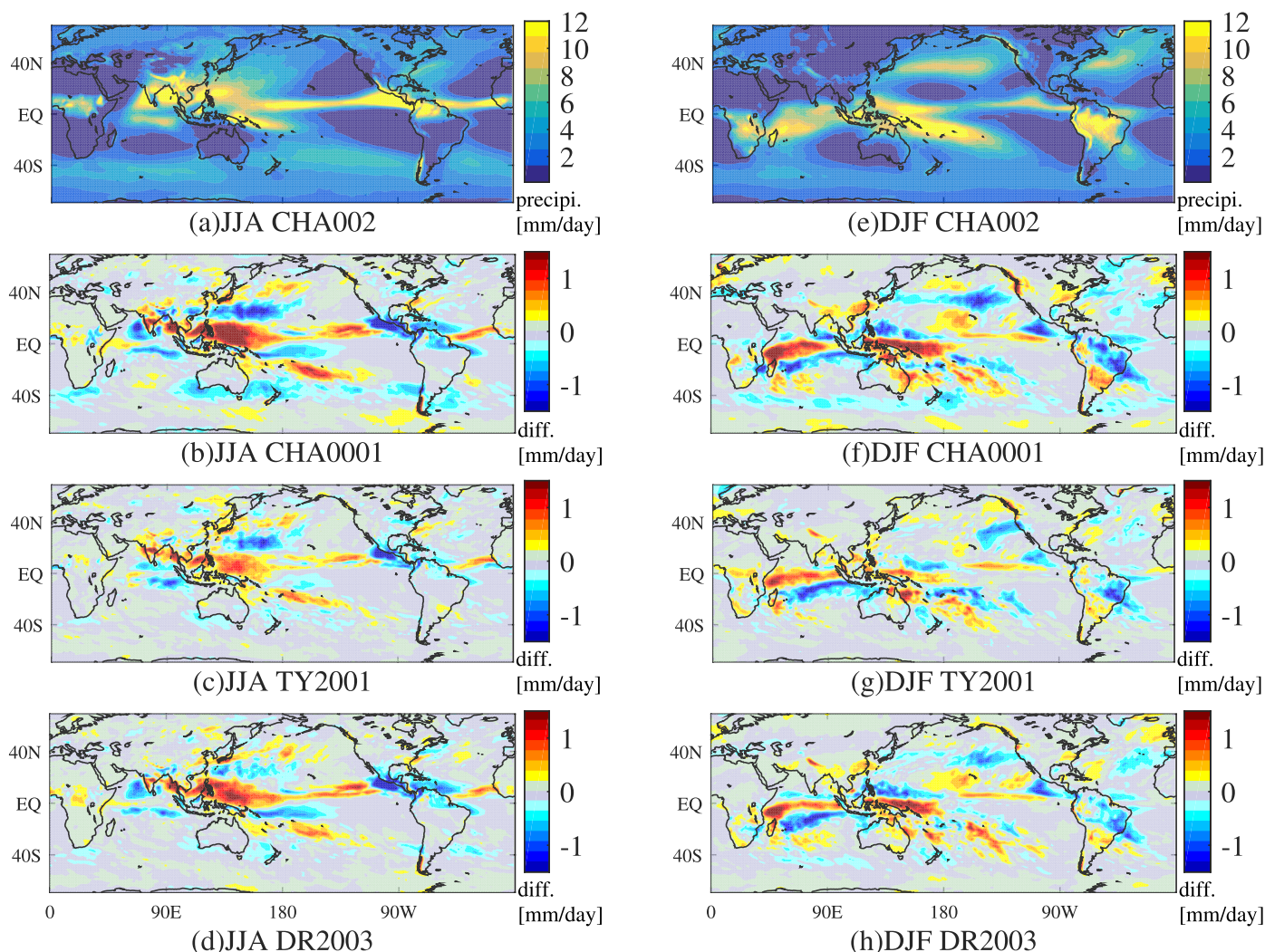


Figure 7. (a) The precipitation climatology (mm/d) in JJA for CHA002. (b–d) The differences (mm/d) between CHA002 and CHA0001, TY2001, and DR2003, respectively. Plots (e–h) are the same as (a–d), but for DJF.

CHA002, and CHA003, respectively; the coefficient for TY2001 and DR2003 are 0.08 and 0.54, respectively. These coefficient represents the magnitude of the differences that can be explained by the EOF first mode. A positive value for the first mode coefficient indicates a strengthening of the Hadley circulation around the Equator (negative anomalies around the Equator) and an equator-ward shift of the ascent region in the Northern Hemisphere (positive anomalies around 15°N). The pattern of Hadley circulation differences (Figure 8b) correspond to pattern of precipitation differences (Figure 8a). Stronger Hadley circulation around the Equator (10°S to 10°N) can contribute to differences in precipitation south and north of the Equator due to an increased south to north water vapor flux.

In the previous section, we described how the implementation of ocean-wave-dependent roughness improved modeling of U_{10} climatology at low latitudes. Here we clarify the relationship between U_{10} climatology and changes in atmospheric circulation. Figure 9 shows the relationship between U_{10} climatology at low latitudes (15°S to 15°N) and the Hadley circulation (represented by the coefficient of the first EOF mode, (a)) and the equatorial north-south differences in precipitation (precipitation from 0 to 15°N minus precipitation from 0 to 15°S, (b)). It is clear that Hadley circulation and precipitation are correlated with U_{10} climatology. The 1 m/s differences at low latitudes in the U_{10} correspond to 0.3 mm/d changes in the equatorial north-south precipitation difference. It is not surprising to find that U_{10} climatology is sensitive to the surface roughness, but it is critical to note that the resulting surface wind differences lead to atmospheric

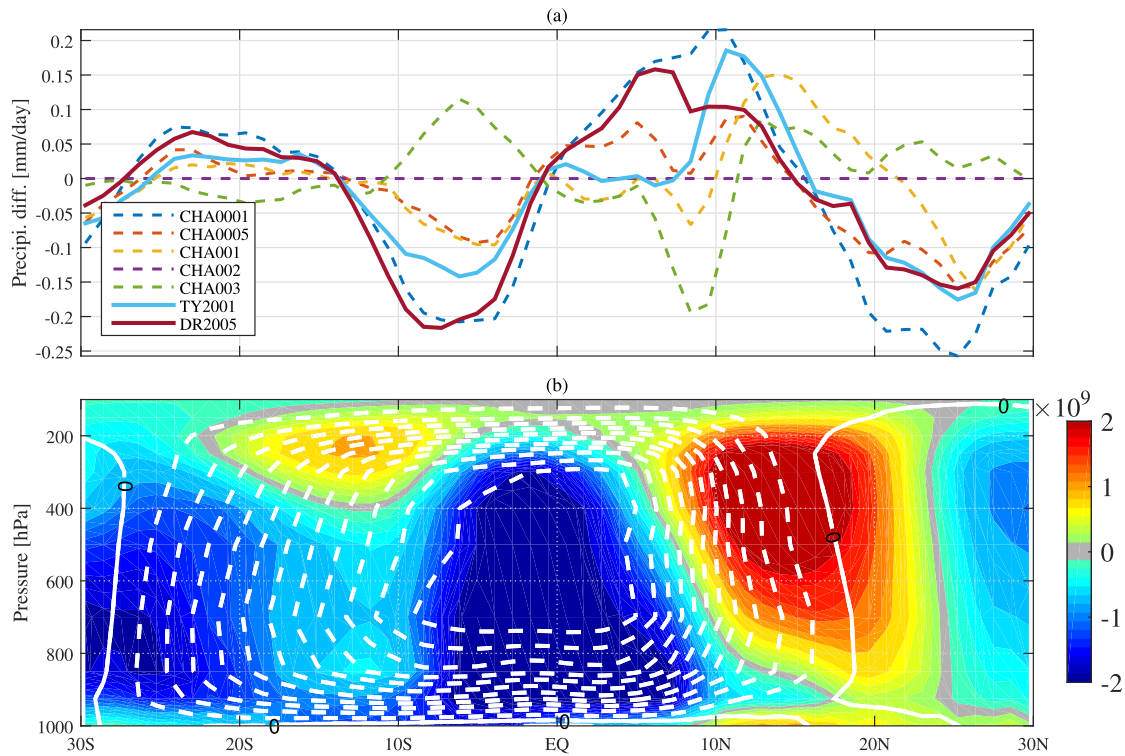


Figure 8. (a) Zonal mean precipitation climatology differences between all the experiments and CHA002 in JJA. (b) Hadley circulation (mass stream functions) in JJA for CHA002 (white contour lines). Dashed contours indicate negative values, and solid contours indicate positive values. The contour interval is 2×10^{10} kg/s. The color shading shows the first EOF mode of the Hadley circulation among seven experiments indicating the representative difference among experiments.

circulation differences, as shown in Figure 9. The sea surface roughness in both experiments with ocean wave-dependent roughness is significantly smaller than in CHA002 (Figure 2b), which drives atmospheric circulation differences. The characteristic pattern of the response of atmospheric circulation to changing

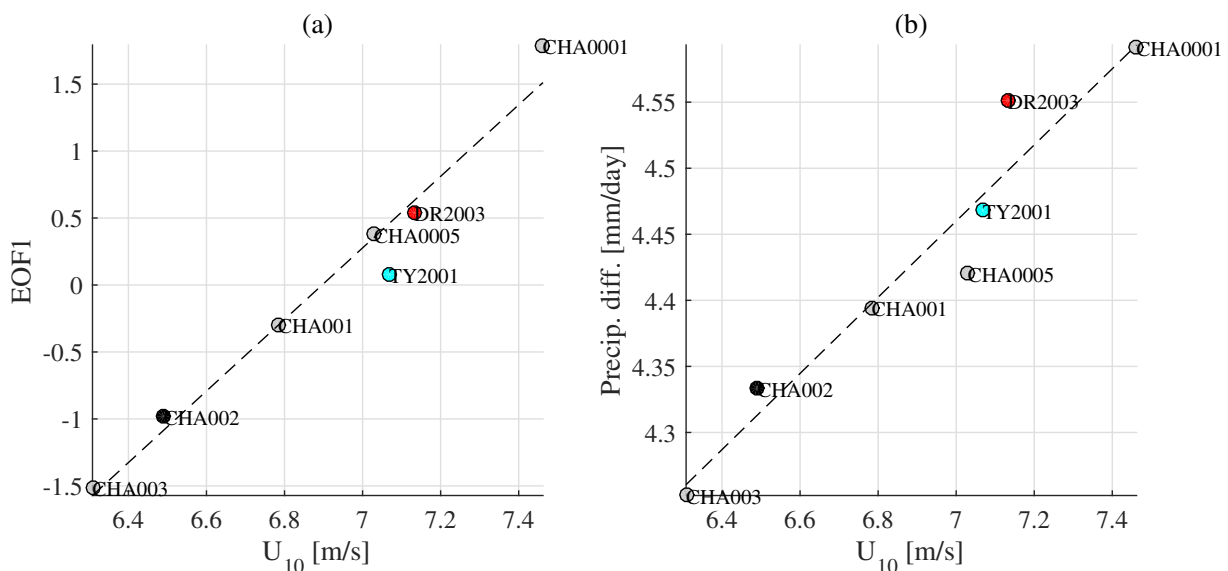


Figure 9. (a) The relationship between U_{10} climatology at low latitudes and the Hadley circulation (represented by the coefficients of first EOF mode). (b) The relationship between U_{10} climatology at low latitudes and the equatorial north-south differences in precipitation.

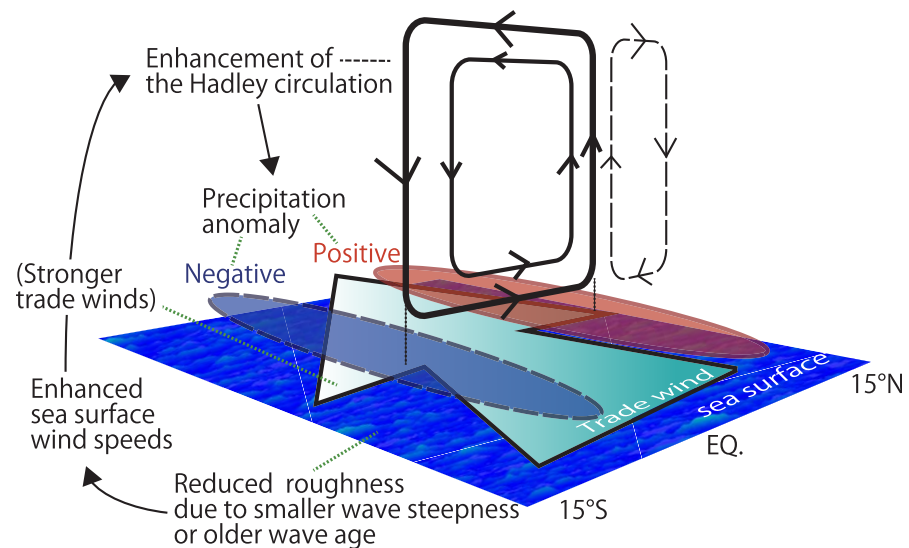


Figure 10. Overview of the atmospheric circulation responses to wave-dependent roughness in the boreal summer.

roughness is seen in Figures 7 and 8. Overview of the atmospheric circulation responses to the wave-dependent roughness is drawn in Figure 10.

3.3.2. DJF Season and the Impact of Swell

The characteristic impact of roughness, and the wind speed differences resulting from it, on atmospheric circulation in the boreal summer was described above. We showed that differences in roughness and wind speed across the entire tropics are important because changes in atmospheric circulation can be entirely described using the average tropical wind speed, as shown in Figure 9; the spatial distribution does not significantly affect atmospheric circulation in boreal summer. The situation is somewhat different in boreal winter. Figures 7e–7h show the boreal winter (DJF) precipitation climatology of CHA002 compared to CHA0001, TY2001, and DR2003. The results of this comparison for DJF are similar to those for JJA, but with the trends reversed. In JJA, we see the negative differences in precipitation south, and positive north, of the Equator with increases in U_{10} (Figure 8a). The negative and positive differences are swapped in DJF. The first EOF mode of the Hadley circulation differences can explain only 60% of the variance in DJF, compared to 87% in JJA. When the EOF analysis is applied to the six experiments excluding TY2001, the percent of the variance explained by the first mode increases significantly to 80%. Figure 11a shows the Hadley circulation difference between TY2001 and CHA002, and Figure 11b shows the first EOF mode of the Hadley circulation among the six experiments excluding TY2001 (this can be compared to Figure 8b for JJA). It is clear that Figures 11a and 11b display different patterns. The spatial pattern of Figure 11a can be characterized by negative anomalies from 0 to 15°S, while Figure 11b shows more positive anomalies around the Equator. This difference between Figures 11a and 11b, smaller positive anomalies around the Equator in TY2001, likely causes the smaller contrast between precipitation south and north of the Equator, especially in the western Pacific (Figure 7g).

This analysis indicates that the differences in Hadley circulation between TY2001 and the other experiments cannot be explained simply by the averaged U_{10} differences across the entire tropical region. The spatial distribution of U_{10} differences (Figure 5c) might have a more substantial effect on Hadley circulation in the boreal winter than in summer. This suggests that swell, represented implicitly in TY2001, impacts the atmospheric circulation; these impacts cannot be represented by wind speed-dependent or wind-sea-dependent roughness (DR2003-like) parameterizations.

The momentum flux between swell and the atmosphere is an open question. It has been reported that wind-following swell can reduce the drag (momentum transfer) coefficient [Drennan *et al.*, 1999; Potter, 2015], but increases have also been reported [Högström *et al.*, 2015]. Also in the case of wind opposed to swell different results have been reported, as an increased drag coefficient [see Drennan *et al.*, 1999; Kudryavtsev and Makin, 2004] or a decreased one in higher wind conditions [García-Nava *et al.*, 2009].

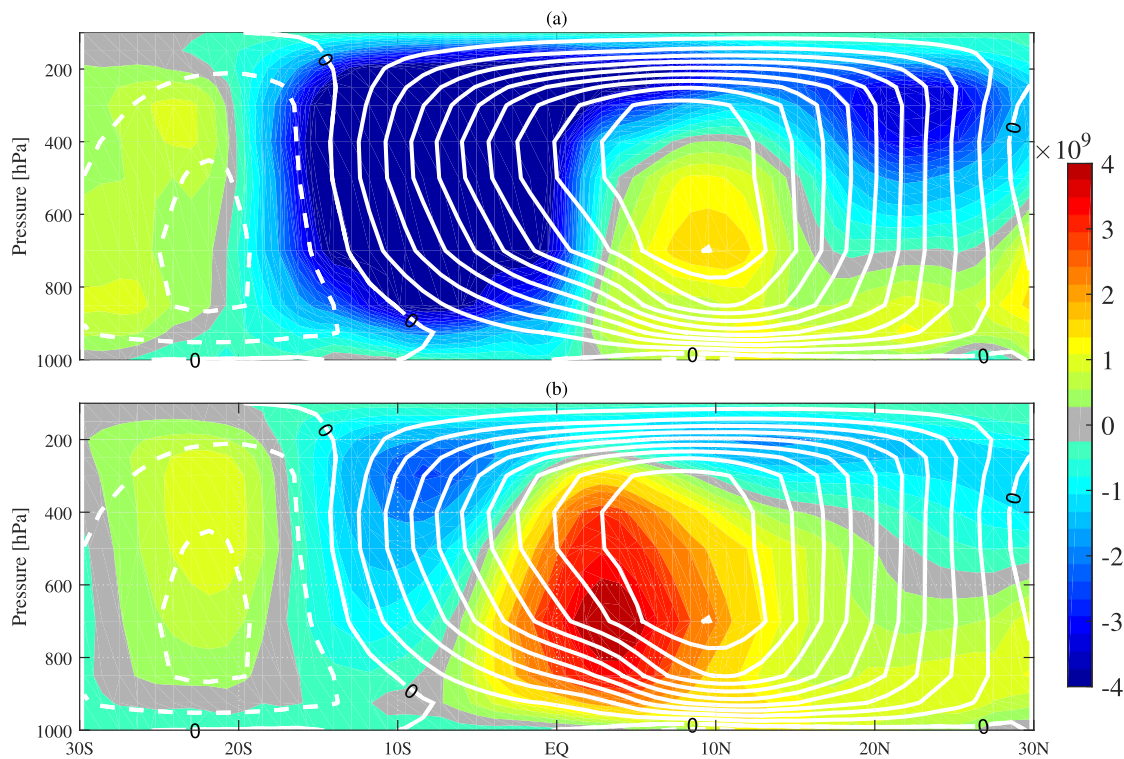


Figure 11. (a) Hadley circulation (mass stream functions) in DJF for CHA002 (white contour lines). Dashed contours indicate negative values, and solid contours indicate positive values. The contour interval is 2×10^{10} kg/s; the color shading shows the difference between CHA002 and TY2001. (b) The first EOF mode of the Hadley circulation among the six experiments excluding TY2001; this is the same as Figure 8b, but for DJF.

TY2001 represents swell information implicitly, and this study indicates that an explicit implementation of swell can impact atmospheric circulation more significantly in the swell dominated (low latitude) area; this impact cannot be explained by wind speed-dependent or wind-sea-dependent roughness. *Wu et al.* [2016] investigated how swell-roughness impacts U_{10} with a wave-atmospheric regional climate model focusing on the European area. Even at such high latitudes, the influences of swell are evident [*Wu et al.*, 2016]. The impact of swell on the climate system needs to be explored and analyzed more deeply.

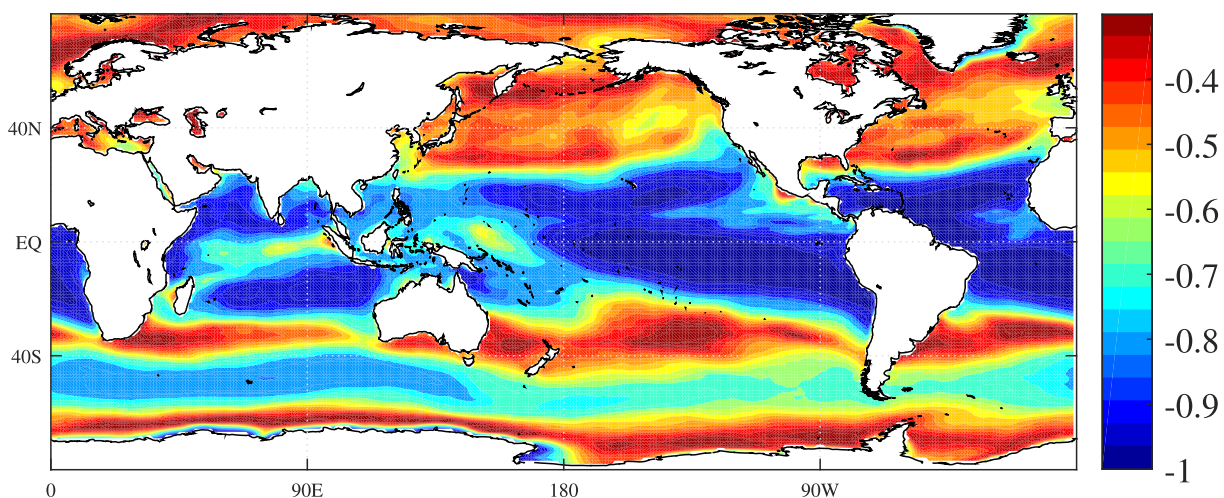


Figure 12. Wind direction stationarity (WDS_{ann}). Note that the value is multiplied by -1 .

4. Conclusions

Ocean surface waves play an important role at an interface between the atmosphere and the ocean. Wave-dependent surface roughness was implemented into the Atmospheric Global Climate Model (MRI-AGCM) using the spectral wave model WAVEWATCH III, and climate simulations were performed. The sea surface roughness within the AGCM was originally defined using the Charnock relation [Charnock, 1955]. Two types of wave-dependent roughness, wave steepness-dependent roughness [Taylor and Yelland, 2001] and wave age-dependent roughness [Drennan et al., 2003], were considered. These two wave-dependent roughness parameterizations are distinct in their definition of the wave spectral peak: the spectral peak of wave steepness-dependent roughness is defined using the total sea, while that of wave age-dependent one is defined using just the wind-sea wave spectrum. The Charnock-like coefficient in Drennan et al. [2003] is a function of the inverse wave age to the power of 1.9, while in Taylor and Yelland [2001] it is a function of inverse wave age to the power of 0.75. The Charnock-like coefficient in Taylor and Yelland [2001] is less affected by inverse wave age and more by swell than that of Drennan et al. [2003]. We also performed climate simulations with simply wind speed-dependent roughness (without a wave model) for comparison with the wave-dependent models.

The bulk momentum transfer coefficients (C_m) under a certain wind speed are almost unique over the global ocean in the climate simulations with wind speed-dependent roughness. In contrast, the climate simulations with wave-dependent roughness showed C_m climatology with clear regional dependence for specific wind speeds. The spatial distribution of C_m corresponded to the dominance of swell in the climate simulations with wave steepness-dependent roughness [Taylor and Yelland, 2001] and the stationarity of wind direction for those with wave age-dependent roughness [Drennan et al., 2003]. Both climate simulations with wave-dependent roughness show marked decreases in roughness (C_m) at low latitudes where swell dominates and wind directions are stationary. The differences in roughness cause 1m/s differences in surface wind climatology compared to the uncoupled simulations; the wind speed enhancement at low latitudes is remarkable, with up to 15% increases. The enhancement of wind speeds at low latitudes leads to an improvement when comparing the simulated wind speed climatology with observations, although wind speeds at high latitudes are overestimated in the models.

The roughness differences can also change atmospheric circulation. The seasonal precipitation climatology varies by 2 mm/d, depending on roughness, and these precipitation changes clearly correspond to changes in Hadley circulation. In the climate simulations with wave-dependent roughness, the reduced roughness and enhanced wind speeds in the tropics (enhanced trade winds) lead to an enhancement of the Hadley circulation. This leads to positive and negative precipitation changes north and south of the Equator, respectively, in the boreal summer (Figure 10); the opposite is true in boreal winter. We also find that swell-dependent roughness impacts atmospheric circulation differently when compared with wind-sea-dependent roughness.

Climate simulations with ocean wave-dependent roughness show improved modeling of surface wind speeds at low latitudes with an overestimation of wind speeds at high latitudes. As shown in Figure 4, the global ocean displays a wide range of climatology and wave characteristics. There are swell dominated areas, wind-sea dominated areas, high and low wave age areas, high and low wave height (wind speed) areas, and so on. Ocean wave-dependent roughness parameterizations applicable to the global ocean with better performances need to be developed; the development and implementation of such parameterizations for GCMs are left for future work.

Appendix A: Wind Direction Stationarity

Wind direction stationarity (WDS) is defined as:

$$WDS = \frac{\sqrt{(\sum^n u)^2 + (\sum^n v)^2}}{\sum^n \sqrt{u^2 + v^2}}, \quad (A1)$$

where u is zonal wind and v is meridional wind component. The numerator in the fraction means a vector average of wind speed and the denominator means a scalar average of wind speed. WDS is smaller with

larger variation in wind direction. If no variation in wind direction, $WDS = 1$. Annual climatology of WDS is written as,

$$WDS_{ann} = \frac{1}{12} \sum_{\text{month}=1}^{12} \frac{\sqrt{(\sum^n u)^2 + (\sum^n v)^2}}{\sum^n \sqrt{u^2 + v^2}}, \quad (\text{A2})$$

where n is the number of 6 hourly outputs in a calendar month. Figure 12 shows the WDS_{ann} derived from 50 years data of DR2003 experiment. Note that the value is multiplied by -1 for the comparison with Figures 3b and 4b.

Acknowledgments

Tomoya Shimura was supported by the Japan Society for the Promotion of Science (JSPS) Fellowship for Young Scientists and Grant-in-Aid for JSPS Fellows (15J07767). This research was supported under the SOUSEI Program by the Ministry of Education, Culture, Sports, Science, and Technology (MEXT). Climate simulation data are available contacting Tomoya Shimura (shimura.tomoya.2v@kyoto-u.ac.jp).

References

- Ardhuin, F., et al. (2010), Semiempirical dissipation source functions for ocean waves. Part I: Definition, calibration, and validation, *J. Phys. Oceanogr.*, *40*(9), 1917–1941.
- Cavaleri, L., B. Fox-Kemper, and M. Hemer (2012), Wind waves in the coupled climate system, *Bull. Am. Meteorol. Soc.*, *93*(11), 1651–1661.
- Charles, E., and M. Hemer (2013), Parameterization of a wave-dependent surface roughness: A step towards a fully coupled atmosphere-ocean-sea ice-wave system, in *13th International Workshop on Wave Hindcasting and Forecasting and 4th Coastal Hazard Symposium*. [Available at <http://www.waveworkshop.org/13thWaves/index.htm>.]
- Charnock, H. (1955), Wind stress on a water surface, *Quart. J. R. Meteorol. Soc.*, *81*(350), 639–640.
- Dee, D., et al. (2011), The ERA-interim reanalysis: Configuration and performance of the data assimilation system, *Quart. J. R. Meteorol. Soc.*, *137*(656), 553–597.
- Drennan, W. M., K. K. Kahma, and M. A. Donelan (1999), On momentum flux and velocity spectra over waves, *Boundary Layer Meteorol.*, *92*(3), 489–515.
- Drennan, W. M., H. C. Graber, D. Hauser, and C. Quentin (2003), On the wave age dependence of wind stress over pure wind seas, *J. Geophys. Res.*, *108*(C3), 8062, doi:10.1029/2000JC000715.
- Drennan, W. M., P. K. Taylor, and M. J. Yelland (2005), Parameterizing the sea surface roughness, *J. Phys. Oceanogr.*, *35*(5), 835–848.
- Fan, Y., S.-J. Lin, I. M. Held, Z. Yu, and H. L. Tolman (2012), Global ocean surface wave simulation using a coupled atmosphere-wave model, *J. Clim.*, *25*(18), 6233–6252.
- Fennig, K., A. Andersson, S. Bakan, C. Klepp, and M. Schröder (2012), Hamburg Ocean Atmosphere Parameters and Fluxes from Satellite Data-HOAPS 3.2-Monthly Means/6-Hourly Composites, Satellite Application Facility on Climate Monitoring, doi:10.5676/EUM_SAF_CM/HOAPS/V001. [Available at https://wui.cmsaf.eu/safira/action/viewDoiDetails?acronym=HOAPS_V001.]
- García-Nava, H., F. Ocampo-Torres, P. Osuna, and M. Donelan (2009), Wind stress in the presence of swell under moderate to strong wind conditions, *J. Geophys. Res.*, *114*, C12008, doi:10.1029/2009JC005389.
- Hasselmann, K., et al. (1973), Measurements of wind-wave growth and swell decay during the Joint North Sea Wave Project (JONSWAP), *Tech. Rep.*, Deutsches Hydrogr. Inst., Hamburg, Germany.
- Hasselmann, S., and K. Hasselmann (1985), Computations and parameterizations of the nonlinear energy transfer in a gravity-wave spectrum. Part I: A new method for efficient computations of the exact nonlinear transfer integral, *J. Phys. Oceanogr.*, *15*(11), 1369–1377.
- Hemer, M. A., and C. E. Trenham (2016), Evaluation of a CMIP5 derived dynamical global wind wave climate model ensemble, *Ocean Modell.*, *103*, 190–203.
- Högström, U., E. Sahlée, A.-S. Smedman, A. Rutgersson, E. Nilsson, K. K. Kahma, and W. M. Drennan (2015), Surface stress over the ocean in swell-dominated conditions during moderate winds, *J. Atmos. Sci.*, *72*(12), 4777–4795.
- Janssen, P. A. E. M. (1991), Quasi-linear theory of wind-wave generation applied to wave forecasting, *J. Phys. Oceanogr.*, *21*(11), 1631–1642.
- Janssen, P. A. E. M., and P. Viterbo (1996), Ocean waves and the atmospheric climate, *J. Clim.*, *9*(6), 1269–1287.
- Jones, I. S., and Y. Toba (2001), *Wind Stress Over the Ocean*, 307 pp., Cambridge Univ. Press, Cambridge, U. K.
- Jungclaus, J., N. Keenlyside, M. Botzet, H. Haak, J.-J. Luo, M. Latif, J. Marotzke, U. Mikolajewicz, and E. Roeckner (2006), Ocean circulation and tropical variability in the coupled model echam5/mpi-om, *J. Clim.*, *19*(16), 3952–3972.
- Kudryavtsev, V. N., and V. K. Makin (2004), Impact of swell on the marine atmospheric boundary layer, *J. Phys. Oceanogr.*, *34*(4), 934–949.
- Luo, J.-J., S. Masson, E. Roeckner, G. Madec, and T. Yamagata (2005), Reducing climatology bias in an ocean-atmosphere CGCM with improved coupling physics, *J. Clim.*, *18*(13), 2344–2360.
- Mizuta, R., et al. (2012), Climate simulations using MRI-AGCM3.2 with 20-km grid, *J. Meteorol. Soc. Jpn.*, *90*(0), 233–258.
- Murakami, H., R. Mizuta, and E. Shindo (2012), Future changes in tropical cyclone activity projected by multi-physics and multi-SST ensemble experiments using the 60-km-mesh MRI-AGCM, *Clim. Dyn.*, *39*, 2569–2584.
- Oort, A. H., and J. J. Yienger (1996), Observed interannual variability in the Hadley circulation and its connection to ENSO, *J. Clim.*, *9*(11), 2751–2767.
- Polichtchouk, I., and T. Shepherd (2016), Zonal-mean circulation response to reduced air-sea momentum roughness, *Quart. J. R. Meteorol. Soc.*, *142*, 2611–2622.
- Potter, H. (2015), Swell and the drag coefficient, *Ocean Dyn.*, *65*(3), 375–384.
- Rayner, N., D. Parker, E. Horton, C. Folland, L. Alexander, D. Rowell, E. Kent, and A. Kaplan (2003), Global analyses of sea surface temperature, sea ice, and night marine air temperature since the late nineteenth century, *J. Geophys. Res.*, *108*(D14), 4407, doi:10.1029/2002JD002670.
- Semedo, A., K. Sušelj, A. Rutgersson, and A. Sterl (2011), A global view on the wind sea and swell climate and variability from era-40, *J. Clim.*, *24*(5), 1461–1479.
- Shie, C., K. Hilburn, L. Chiu, R. Adler, I. Lin, E. Nelkin, J. Ardizzone, and S. Gao (2012), *Goddard Satellite-Based Surface Turbulent Fluxes, Daily Grid, Version 3*, Goddard Earth Sci. Data and Inform. Serv. Center (GES DISC), Greenbelt, Md.
- Shimura, T., N. Mori, and M. Hemer (2016), Variability and future decreases in winter wave heights in the Western North Pacific, *Geophysical Res. Lett.*, *43*, 2716–2722.
- Taylor, P. K., and M. J. Yelland (2001), The dependence of sea surface roughness on the height and steepness of the waves, *J. Phys. Oceanogr.*, *31*(2), 572–590.

- Toba, Y. (1972), Local balance in the air-sea boundary processes, *J. Oceanogr. Soc. Jpn.*, 28(3), 109–120.
- Tolman, H. (2014), User manual and system documentation of WAVEWATCH III version 4.18, Tech. Note, 316, 282 pp., NOAA/NWS/NCEP/MMAB, College Park, Md.
- Von Storch, H., and F. Zwiers (2002), *Statistical Analysis in Climate Research*, 484 pp., Cambridge Univ. Press, Cambridge, U. K.
- Weber, S. L., H. von Storch, P. Viterbo, and L. Zambresky (1993), Coupling an ocean wave model to an atmospheric general circulation model, *Clim. Dynam.*, 9(2), 63–69.
- Wu, L., A. Rutgersson, E. Sahlée, and X. G. Larsén (2016), Swell impact on wind stress and atmospheric mixing in a regional coupled atmosphere-wave model, *J. Geophys. Res. Oceans*, 121, 4633–4648, doi:10.1002/2015JC011576.
- Yasuda, T., S. Nakajo, S. Kim, H. Mase, N. Mori, and K. Horsburgh (2014), Evaluation of future storm surge risk in east asia based on state-of-the-art climate change projection, *Coastal Eng.*, 83, 65–71.
- Yu, L., X. Jin, and R. Weller (2008), Multidecade global flux datasets from the Objectively Analyzed Air-sea Fluxes (OAFlux) Project: Latent and sensible heat fluxes, ocean evaporation, and related surface meteorological variables, *OAFlux Project Tech. Rep.OA-2008-01*, Woods Hole Oceanogr. Inst., Wood Hole, Mass.
- Zhang, H.-M., J. J. Bates, and R. W. Reynolds (2006), Assessment of composite global sampling: Sea surface wind speed, *Geophys. Res. Lett.*, 33, L17714, doi:10.1029/2006GL027086.